Title
Nitrogen dioxide at the airâ��water interface: trapping, absorption, and solvation in the bulk and at the surface

Journal
Physical Chemistry Chemical Physics, 15(1)

ISSN
1463-9076 1463-9084

Authors
Murdachaew, Garold
Varner, Mychel E
Phillips, Leon F
et al.

Publication Date
2013

DOI
10.1039/c2cp42810e

Peer reviewed

PCCP

RSC Publishing

PAPER

View Article Online
View Journal | View Issue

Cite this: *Phys. Chem. Chem. Phys.*, 2013, **15**, 204

Nitrogen dioxide at the air–water interface: trapping, absorption, and solvation in the bulk and at the surface

Garold Murdachaew,†*[ab] Mychel E. Varner,[b] Leon F. Phillips,[c] Barbara J. Finlayson-Pitts[b] and R. Benny Gerber[ab]

Received 11th August 2012,
Accepted 31st October 2012

DOI: 10.1039/c2cp42810e

www.rsc.org/pccp

The interaction of NO_2 with water surfaces in the troposphere is of major interest in atmospheric chemistry. We examined an initial step in this process, the uptake of NO_2 by water through the use of molecular dynamics simulations. An NO_2–H_2O intermolecular potential was obtained by fitting to high-level *ab initio* calculations. We determined the binding of NO_2–H_2O to be about two times stronger than that previously calculated. From scattering simulations of an NO_2 molecule interacting with a water slab we observed that the majority of the scattering events resulted in outcomes in which the NO_2 molecule became trapped at the surface or in the interior of the water slab. Typical surface-trapped/adsorbed and bulk-solvated/absorbed trajectories were analyzed to obtain radial distribution functions and the orientational propensity of NO_2 with respect to the water surface. We observed an affinity of the nitrogen atom for the oxygen in water, rather than hydrogen-bonding which was rare. The water solvation shell was less tight for the bulk-absorbed NO_2 than for the surface-adsorbed NO_2. Adsorbed NO_2 demonstrated a marked orientational preference, with the oxygens pointing into the vacuum. Such behavior is expected for a mildly hydrophobic and surfactant molecule like NO_2. Estimates based on our results suggest that at high NO_2 concentrations encountered, for example, in some sampling systems, adsorption and reaction of NO_2 at the surface may contribute to the formation of gas-phase HONO.

1 Introduction

Nitrogen dioxide is a well-known air pollutant for which air quality standards are set. Photolysis of NO_2 is the sole known anthropogenic source of O_3 in the troposphere, which is of interest because ozone is also a toxic air pollutant, serves as an oxidant source in the atmosphere, and is a greenhouse gas.[1] While the gas phase reactions of NO_2 are reasonably well understood, its interactions with water are not. It is known, for example, that NO_2 interacts with water on surfaces in the lower atmosphere to generate nitrous acid (HONO).[2–6] This is important in air because HONO rapidly photolyzes to form the highly reactive OH radical that drives the chemistry of the atmosphere.[1,3] However, despite the importance of this process, the kinetics and mechanisms of the NO_2 interaction with water to form HONO are not well understood.

One proposed mechanism for HONO formation in the dark involves the heterogeneous hydrolysis of NO_2, which stoichiometrically (but certainly not mechanistically) is summarized in eqn (1):

$$2NO_2 + H_2O \rightarrow HONO + HNO_3. \quad (1)$$

This process could proceed *via* the initial formation of the NO_2 dimer in the gas phase followed by its reaction with surface water, likely *via* an $NO^+NO_3^-$ intermediate.[7–14] Alternatively, it could occur *via* the uptake of NO_2 as the monomer at the water surface. If the adsorbed NO_2 has sufficient residence time on the surface, it could undergo further reaction with a second NO_2 either from the gas phase or by diffusion from the sub-surface liquid. The possible role of the dimer has been probed through both experimental and theoretical studies,[7–15] and certainly may contribute at higher NO_2 concentrations where the dimer can be formed from the monomer in the gas phase. However, the issue of whether the residence time of NO_2 at a water surface suffices for developing sufficient concentrations to undergo subsequent reactions at the surface has not been examined yet, to the best of our knowledge.

[a] *Institute of Chemistry and the Fritz Haber Research Center for Molecular Dynamics, Hebrew University, Jerusalem 91904, Israel*
[b] *Department of Chemistry, University of California, Irvine, CA 92697, USA*
[c] *Department of Chemistry, University of Canterbury, Private Bag 4800, Christchurch, New Zealand*
† Present address: Department of Chemistry, University of Helsinki, P. O. Box 55, FIN-00014, Finland. E-mail: garold.murdachaew@helsinki.fi; Fax: +358 (0)9 191 50279; Tel: +358 (0)9 191 50318.

Our objectives were to study the possible adsorption or absorption of an NO_2 molecule at the air/water interface and to determine whether such a process is relevant to atmospheric chemistry. Therefore we report here studies of the interaction of NO_2 with liquid water through scattering and equilibrium simulations using molecular dynamics (see, *e.g.*, ref. 16–19 for analogous work). For the pairwise interaction of NO_2–H_2O, we fitted a rigid-monomer non-polarizable intermolecular potential to accurate *ab initio* NO_2–H_2O interaction energies obtained using the symmetry-adapted perturbation theory (SAPT) for the intermolecular interactions method. We then selected a suitable H_2O–H_2O intermolecular potential which is known to correctly describe water structure, hydrogen bond populations, and internal energy, amongst other properties, in both the bulk and at the surface. The SPC/E[20] water model fits these requirements at low cost. Both intermolecular potentials can be characterized as effective potentials since the many-body polarization is taken into account by the use of increased values of the dipole moments of H_2O and NO_2.

The paper is organized as follows. Systems and methods used are described first (Section 2), followed by results (Section 3), implications for atmospheric chemistry (Section 4), and concluding remarks (Section 5).

2 Systems and methods

2.1 Development of the NO_2–H_2O potential

An initial step was to select a model of water to be used with our NO_2–H_2O potential in simulations of systems containing multiple water molecules. The SPC/E[20] rigid-monomer potential (see Table 1) gives a good and computationally efficient description of bulk and interfacial water. It is of the site–site Lennard-Jones plus electrostatics type,

$$V = \sum_{ab}\left[4\varepsilon_{ab}\left(\left(\frac{\sigma_{ab}}{R_{ab}}\right)^{12}-\left(\frac{\sigma_{ab}}{R_{ab}}\right)^{6}\right)+\frac{q_a q_b}{R_{ab}}\right]. \qquad (2)$$

The terms in eqn (2) account for repulsion, dispersion (and induction), and electrostatic interactions (through the partial charges), respectively. Indices *a* and *b* refer to sites on different monomers. The parameters of this potential and other details are given in Table 1.

In calculating the NO_2–H_2O potential we also took the monomers to be rigid in the *ab initio* calculations and in the fit. The experimental geometries of NO_2 and H_2O were used in the *ab initio* calculations while the SPC/E geometry of H_2O was used in the fit. Since the internal bonds are stiff, the use of rigid monomers is a good approximation and moreover has the effect of reducing the necessary sampling for the potential fit from 12 D to 6 D. Thirty-one angular configurations were selected in addition to the C_s symmetry global minimum angular configuration and radial scans were performed at all configurations. The final number of *ab initio* points used in the fit was 381.

Table 1 Parameters of the SPC/E[20] H_2O–H_2O intermolecular potential[a]

Site type a	Site type b	q^b [au]	ε [kcal mol^{-1}]	σ [Å]
O_w		−0.8476		
H_w		0.4238		
O_w	O_w		0.155	3.166

[a] r_{OH} = 1.0 Å and θ_{HOH} = 109.47° (the corresponding measured values[21] are $r_{e,exp}$ = 0.9572 Å, $\theta_{e,exp}$ = 104.52°). Omitted site–site parameters have a value of zero. [b] The dipole moments of water with this non-polarizable but effective potential in the gas and in the liquid are the same, $\mu_{gas} = \mu_{liq}$ = 2.35 D [the accepted values are μ_{gas} = 1.850 D (measured)[22] and $\mu_{liq} \approx$ 2.65–3 D (estimated[23–25] from experiment and *ab initio* simulation)].

The symmetry-adapted perturbation theory (SAPT) for intermolecular interactions, newly extended to open-shell species, was used to explore the potential energy surface. The efficient implementation used relies on a density-functional theory (DFT) description of the monomers and thus is called SAPT(DFT).[28–31] Open-shell SAPT has been used to study atmospherically-relevant complexes with good results, see, *e.g.*, ref. 30. The PBE0[32] exchange-correlation functional was used for the monomers and the electronic densities of the monomers were corrected using the vertical ionization potentials from the NIST database[33] for H_2O (I = 0.4638 Hartree) and calculated by us for NO_2 with UKS-PBE0/aug-cc-pVQZ using MOLPRO[34] (doublet to singlet, I^{α} = 0.4294 Hartree; doublet to triplet, I^{β} = 0.4769 Hartree).

The total (hybrid) SAPT(DFT) interaction energy is composed of the following terms:

$$E_{int}^{SAPT} = \left(E_{elst}^{(1)}\right) + \left(E_{exch}^{(1)}\right) + \left(E_{ind}^{(2)} + \tilde{E}_{exch-ind}^{(2)} + \delta E_{int,resp}^{HF}\right) + \left(E_{disp}^{(2)} + \tilde{E}_{exch-disp}^{(2)}\right). \qquad (3)$$

As in ref. 35, we have grouped the second-order exchange components with their respective non-exchange counterparts. Some explanation on the grouping and meaning of individual components can be found in ref. 35, as well as in ref. 28–31. Subsequently, we will refer to the terms in parentheses simply as the electrostatics, exchange, induction, and dispersion energies, respectively. The division of the interaction energy into physically interpretable components enabled by SAPT is helpful in understanding weakly-bound complexes.

The fit is based on SAPT(DFT)/aTZ+3322 *ab initio* points, where the notation indicates that the aug-cc-pVTZ basis set on atoms was supplemented with a set of 3s3p2d2f basis functions on the midpoint between the centers of mass of NO_2 and H_2O (see ref. 30 for details). We will employ the shortened notation a*X*Z, where X = 2, 3, and 4 refer to the Dunning basis sets[36] aug-cc-pVDZ, aug-cc-pVTZ, and aug-cc-pVQZ, respectively. Adding a midbond basis set is known to accelerate basis set convergence in van der Waals complexes at lower cost than increasing the atomic basis set. The fit form was of the site–site, exp-6 plus electrostatics type,

$$V = \sum_{ab}\left[A_{ab}e^{-B_{ab}R_{ab}} - \frac{C_6^{ab}}{R_{ab}^6} + \frac{q_a q_b}{R_{ab}}\right], \qquad (4)$$

the same model as that used for this complex in ref. 27. However, to better fit the *ab initio* points, we placed an additional virtual site (labeled M) on the NO_2 bisector, close to the N atom. Similarly, an M_w (uncharged) site was placed on each water molecule to better model its interaction with NO_2. Note that not all sites are involved in all interactions. We used the fixed partial charges from ref. 27 which reproduce the (enhanced) dipole moment of NO_2 in liquid water.

Table 2 Parameters of the NO_2–H_2O intermolecular potential (fit) obtained in this work[a]

Site type a	Site type b	q[b] [au]	A [kcal mol^{-1}]	B [Å^{-1}]	C_6 [kcal mol^{-1} Å^6]
N		0.28			
O		−0.14			
M		0.0			
O_w	N		27956.0585	3.5196	2493.0559
O_w	O		13188.9550	3.3825	198.9990
O_w	M		90474.3281	4.1831	0.0
H_w	N		−926.9366	2.2456	0.0
H_w	O		5585.6072	4.5674	0.0
H_w	M		2487.2566	2.6495	0.0
M_w	N		11751.1798	2.5409	0.0
M_w	O		6417.5834	3.5139	0.0
M_w	M		−25690.9038	2.9305	0.0

[a] For NO_2, we used the experimental geometry[26] $r_{NO} = r_{e,exp} = 1.193$ Å, $\theta_{ONO} = \theta_{e,exp} = 134.1°$. An M site was placed 0.171 Å from the nitrogen atom along the ONO bisector. The H_2O molecule is modeled by the SPC/E intermolecular potential as described in Table 1 but we have also placed an M_w site 0.212 Å from the oxygen atom along the HOH bisector for the use of the SPC/E potential with NO_2. [b] The dipole moments of the NO_2 molecule with this non-polarizable but effective potential in the gas phase and solvated in water are the same, $\mu_{gas} = \mu_{aq} = 0.63$ D, which was obtained by fitting the NO_2 partial charges to the dipole moment of NO_2 solvated in a water cluster in the simulations of Galashev and Rakhmanova[27] (note that the measured[26] gas phase value is 0.33 D).

During the fitting procedure we observed that some of the C_6 site–site parameters obtained were small (or even negative, an unphysical situation). Thus, these were constrained to be zero and finally only two C_6 parameters were required. The fitted parameters and additional details are given in Table 2.

2.2 Simulations of extended systems

The classical force field simulations were done using the FIST module within the CP2K package.[37] The molecular dynamics simulations of scattering were performed in the microcanonical (*NVE*) ensemble with initial velocities assigned from the Maxwell–Boltzmann distribution at 300 K. The system consisted of a periodic rectangular box with dimensions of $15.00 \times 15.00 \times 71.44$ Å^3, with the long axis of the box along the $\hat{Z}$ direction. A slab of 216 water molecules (thickness of about 30 Å) was located at the center of the box, bound on either surface along the $\hat{Z}$ direction by vacuum. A single NO_2 molecule was introduced in the scattering simulations. Such a water system is sufficient for modeling both bulk and interfacial conditions.[38–40] It is known that the SPC/E potential yields a density very close to 1 g cm^{-3} at the center of the slab, as well as reproducing conditions at the interface.[39] Rigid molecule constraints were imposed using the SHAKE algorithm.[41] We started with well-equilibrated water configurations from ref. 40 and as in ref. 28 and 39 confirmed that the correct density and hydrogen bond population profiles are obtained for the pure water system. As in ref. 40, the density profile with the height Z from the vertical center of the slab was fitted using

$$\rho(Z) = \frac{1}{2}(\rho_l + \rho_v) - \frac{1}{2}(\rho_l - \rho_v)\tanh\left(\frac{Z - Z_{GDS}}{\delta}\right), \quad (5)$$

where $Z = 0$ is the center of the slab; ρ_l and ρ_v are the liquid and vapor densities, respectively (the latter is taken to be zero); Z_{GDS} is the position of the Gibbs dividing surface (taken to be the point where the density is half that of the liquid density); and δ is the interfacial width (the 10%–90% thickness is 2.1972δ). We obtained for the SPC/E potential $\rho_l = 0.962$ g cm^{-3}, $Z_{GDS} = 14.908$ Å, and $\delta = 1.007$ Å.

For each of the 160 trajectories, the NO_2 molecule was released at 10 Å above the water surface but in a different orientation and position in the plane. Additionally, a slightly different equilibrated water structure was used in each case. Smooth particle mesh Ewald summations were used to sum electrostatic contributions. The time step was 1 fs and each trajectory was propagated for 90 ps. The determination of the fate of an NO_2 molecule impacting on the surface was based on the average height of the N atom above the center of the water slab in the last 10 ps at the end of a 90 ps simulation: scattered (in the vacuum, $Z > Z_{GDS} + 2\delta$ after interacting with the surface for 2 ps or less), adsorbed ($Z_{GDS} - 2\delta \leq Z \leq Z_{GDS} + 2\delta$), desorbed (in the vacuum, $Z > Z_{GDS} + 2\delta$ after first having adsorbed or absorbed for more than 2 ps), or absorbed (in the bulk, $Z < Z_{GDS} - 2\delta$). The N atom was used for convenience; the use of the center-of-mass of NO_2 made no discernable difference. The thermal (S) and mass (α) accommodation coefficients were calculated from the numbers of NO_2 trajectories with the various outcomes (as recommended in ref. 18): S = (number of impinging molecules equilibrated to liquid temperature)/(number of molecules impinging on the liquid surface), or

$$S = \frac{n_{desorbed} + n_{adsorbed} + n_{absorbed}}{n_{scattered} + n_{desorbed} + n_{adsorbed} + n_{absorbed}}, \quad (6)$$

and α = (number of impinging molecules solvated in the liquid)/(number of molecules impinging on the liquid surface), and

$$\alpha_{upper} = \frac{n_{adsorbed} + n_{absorbed}}{n_{scattered} + n_{desorbed} + n_{adsorbed} + n_{absorbed}}, \quad (7)$$

where α_{upper} gives an upper limit for the mass adsorption coefficient. A better estimate (but still an upper limit since most simulations are of limited duration compared to experimental time scales) of the longer-time mass accommodation coefficient can be made by considering the relative probability of the possible eventual absorption (rather than desorption) of adsorbed molecules (see, *e.g.*, ref. 18)

$$p_k = \frac{n_{absorbed}}{n_{desorbed} + n_{absorbed}}, \quad (8)$$

and thus finally

$$\alpha = \frac{p_k \times n_{adsorbed} + n_{absorbed}}{n_{scattered} + n_{desorbed} + n_{adsorbed} + n_{absorbed}}. \quad (9)$$

A typical "adsorbed" and a typical "absorbed" trajectory were further extended up to about 0.5 ns in the canonical (*NVT*) ensemble (with Nosé–Hoover "massive" thermostatting)[42,43] at 300 K and used to obtain (equilibrium) structural properties. All other settings were identical to those in the *NVE* calculations.

3 Results and discussion

3.1 NO_2–H_2O

3.1.1 Benchmarks and nature of bonding. There are a small number of *ab initio* studies of the weakly-bound $NO_2(\tilde{X}^2A_1)$–H_2O complex, either in the gas phase or solvated with additional water molecules.[44–46] The global minimum has been found to be a non-hydrogen-bonded C_s structure, with the nitrogen of NO_2 closest to the oxygen of water.[45,46] The C_s structure of ref. 44 which found the oxygens of NO_2 to be closer to the hydrogens of water is likely due to the use of a basis set that was too small. An empirical potential[27,47] used in previous molecular dynamics simulations of NO_2 molecules in water clusters had an NO_2–H_2O bond of only -1.07 kcal mol^{-1} at the C_{2v} symmetry structure and a too-long R_{N-O_w} separation of 3.24 Å.

Our geometry optimization of the NO_2–H_2O complex at the coupled-cluster singles and doubles level of theory with a perturbative treatment of triples, an unrestricted Hartree–Fock reference wave function, and the basis set aug-cc-pVTZ (UHF-CCSD(T)/aug-cc-pVTZ or CCSD(T)/aTZ for short) also yielded an optimized structure of C_s symmetry with an R_{N-O_w} separation of 2.82 Å. Other levels of theory (HF, MP2, or CCSD; also DFT using BLYP-D2 and B3LYP-D2, where an empirical dispersion correction[48] is used, all with the unrestricted reference wave functions, and basis sets of at least aDZ quality) yielded a very similar structure. The C_s global minimum (and a C_{2v} secondary minimum structure, see below) and the interaction energies are presented in Fig. 1(a) and Table 3. Spin-contamination in the unrestricted Hartree–Fock calculations was not severe (S^2 values of 0.77). Comparison of relative CCSD(T) energies from unrestricted and restricted open-shell calculations yielded values with differences less than 0.01 kcal mol^{-1}, as Table 3 shows.

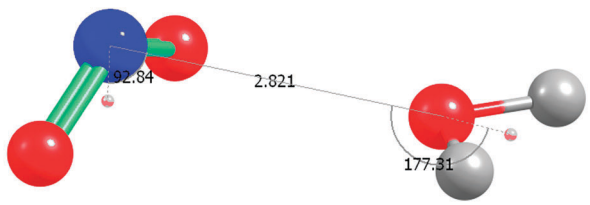

(a) Global minimum structure has C_s symmetry (R_{N-O_w} = 2.821 Å, $\theta_1 = 92.84°$, $\theta_2 = 177.31°$)

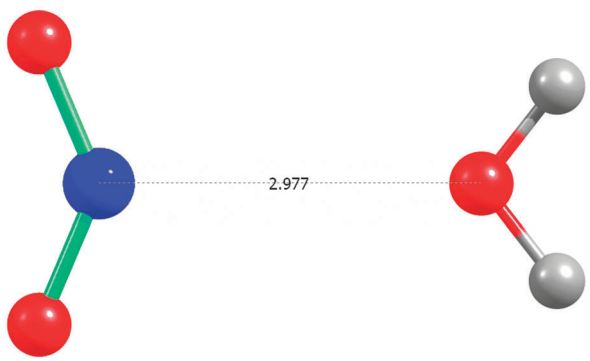

(b) A secondary minimum structure with C_{2v} symmetry (R_{N-O_w} = 2.977 Å, $\theta_1 = 180°$, $\theta_2 = 180°$)

Fig. 1 NO_2–H_2O structures from CCSD(T)/aTZ geometry optimizations.

Table 3 Characteristics of two critical points in the minimum energy region of the NO_2–H_2O potential energy surface. See also Fig. 1. As in the figure, the angles (θ_1,θ_2) in CCSD(T)/aTZ geometry-optimized C_s and C_{2v} configurations are (92.84°, 177.31°) and (180°, 180°), respectively[a]

	(a) C_s		(b) C_{2v}	
Method	R_{N-O_w} [Å]	E_{int} [kcal mol^{-1}]	R_{N-O_w} [Å]	E_{int} [kcal mol^{-1}]
HF/aTZ	2.821	−1.45	2.977	−1.24
HF/aQZ	2.821	−1.40	2.977	−1.19
MP2/aTZ	2.821	−2.22	2.977	−0.96
MP2/aQZ	2.821	−2.15	2.977	−0.89
RCCSD(T)/aTZ	2.821	−2.38	2.977	−1.35
CCSD(T)/aTZ	2.821	−2.38	2.977	−1.36
CCSD(T)/aQZ	2.821	−2.30	2.977	−1.27
CCSD(T)(CBS)[b]	2.821	−2.26	2.977	−1.22
SAPT(DFT)/aTZ+3322	2.821	−2.30	2.977	−1.30
Fit (Galashev and Rakhmanova[27])	2.821	0.68	2.977	−0.88
Opt	2.89	−0.74	3.24	−1.07
Fit (this work)	2.821	−2.10	2.977	−2.45
Opt	2.89	−2.25	2.88	−2.48
BLYP-D2/DZ	2.821	−1.55	2.977	−0.21
BLYP-D2/aDZ	2.821	−0.23	2.977	0.56
Opt	2.94	−1.70	3.03	−0.86
B3LYP/aDZ	2.821	−1.15	2.977	−0.54
Opt	2.95	−1.36	3.15	−0.69
B3LYP-D2/aDZ	2.821	−2.08	2.977	−1.13
Opt	2.86	−2.19	2.97	−1.22
B3LYP-D2/aTZ	2.821	−2.06	2.977	−1.13
Opt	2.89	−2.13	3.00	−1.16

[a] Unless otherwise indicated [*e.g.*, RCCSD(T)], unrestricted open-shell Hartree–Fock or Kohn–Sham reference wave functions are used for the *ab initio* calculations (but SAPT uses the restricted open-shell Kohn–Sham reference wave function). The *ab initio* interaction energies are without counterpoise (CP) correction (but the supermolecular portion of the SAPT interactions energy, $\delta E^{HF}_{int,resp}$, is CP-corrected; also, all SAPT calculations use the full dimer basis set). The frozen core (fc) approximation was used for the supermolecular *ab initio* correlation energy calculations [but the correlation part of the SAPT energy is all-electron (ae)]. MP2 and CCSD(T) interaction energies are fc at the CCSD(T)(ae)/aTZ optimized geometries. Geometries are re-optimized with the given method if marked "opt". Coupled-cluster geometry optimizations were performed with CFOUR.[49] The DFT calculations and geometry optimizations were performed with NWCHEM.[50] CP2K[37] was used for the empirical fit calculations and rigid-monomer geometry optimizations (using simulated annealing). The fits use rigid monomers with the SPC/E and the experimental monomer geometries for H_2O and NO_2, respectively. [b] $E^{CCSD(T)}_{int}(CBS) = E^{HF}_{int}(X+1) + \Delta E^{CCSD(T)}_{int}(X+1, X)$ where the correlated term was extrapolated using the standard X^{-3} two-point formula[51] and the basis sets aug-cc-pV(X+1, X)Z are aQZ and aTZ.

Extrapolation to the complete basis set (CBS) limit of the CCSD(T) energies was performed using the aTZ and aQZ basis set results. As expected, these interaction energies without the counterpoise correction smoothly approach the CBS limit from below. The NO_2–H_2O complex is about twice as strongly bound as previously determined, with a binding energy of -2.26 kcal mol^{-1} as determined by CCSD(T)/CBS. Note that the SAPT interaction energies agree very well with the CCSD(T)/CBS benchmarks. To compare with results using DFT, we performed also DFT geometry minimizations and found that, perhaps fortuitously, B3LYP-D2 with aDZ and aTZ basis sets also closely reproduces the benchmark structures and binding energies.

The binding energy of only about −0.90 kcal mol^{-1} found in ref. 45, where the authors used B3LYP/6-311+G(2d,p), is apparently due to authors' neglect of a dispersion contribution, which is important for this complex.

We found a secondary structure of C_{2v} symmetry that is bound by −1.22 kcal mol^{-1}. See Fig. 1(b) and Table 3 for details. A hydrogen-bonded *trans* structure ONO–HOH, yet another secondary structure, which the authors of ref. 45 found to be almost of the same depth as their C_s global minimum, we found to also be about 1 kcal mol^{-1} less attractive than our global minimum. Our further exploration of the NO_2–H_2O potential energy surface (PES) showed that it is flat in the region of the minimum with respect to a symmetry-breaking wag of the H_2O molecule; *i.e.*, in the transition from the C_s to a nearby C_1 structure.

Both the C_s and C_{2v} structures optimize electrostatic interactions (based on consideration of the dipole–dipole interaction or interaction of partial charges fitted to the multipole moments). Our SAPT component analysis is presented in Fig. 2, as the total interaction energies from SAPT and CCSD(T)/CBS. Note that the SAPT interaction energy is in very good agreement with CCSD(T). With respect to components of the interaction energy, the electrostatics component is dominant in the bonding and is the reason for the formation of an N–O_w bond (rather than some form of hydrogen bond, *e.g.*, O–H_w). We will see that this bonding has possible implications for NO_2 dimerization and the subsequent hydrolysis. The dispersion component is significant in adding to the depth of the PES, as is also confirmed by comparing the interaction energies obtained by B3LYP and B3LYP-D2 methods. Since the electrostatics component, being directional, will be rotationally averaged during the thermal motions of molecules, components that are more isotropic, like dispersion, will continue to be essential in determining the average minimal structures during MD simulations.

3.1.2 NO_2–H_2O fit. Fig. 3 presents a radial scan of the interaction energy through the C_s configuration while Table 2 presents the parameters of the potential fitted in this work. Within the important low-energy regions, most relevant to molecular dynamics, our fit reproduces the *ab initio* points very well. Although the errors are sometimes larger at the other 31 angular

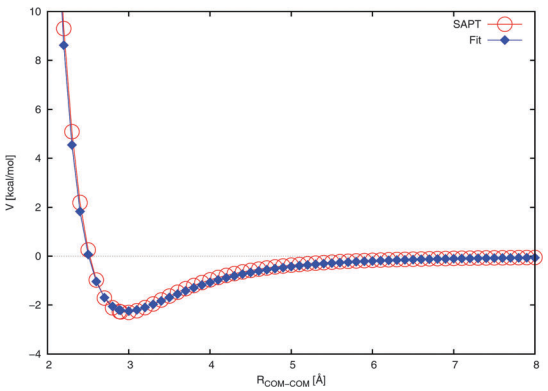

Fig. 3 Radial cut through the NO_2–H_2O potential energy surface at the C_s angular configuration (see Fig. 1(a)). The fit is compared to the *ab initio* calculated interaction energies. The lines are drawn to guide the eye.

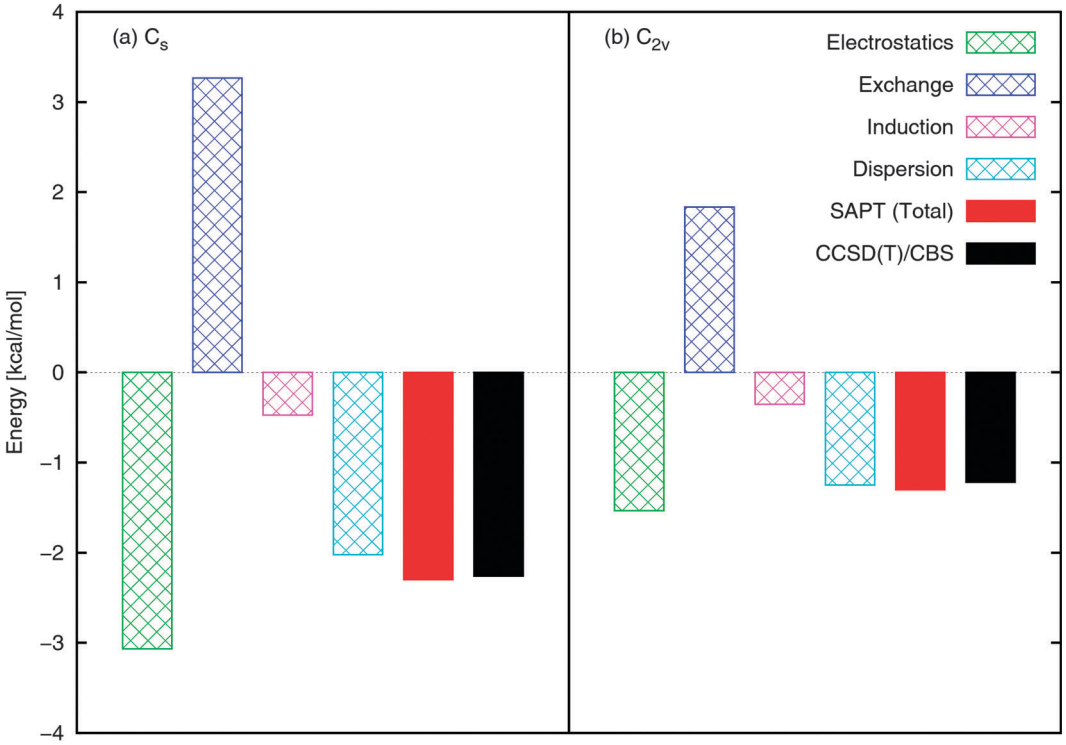

Fig. 2 NO_2–H_2O SAPT interaction energy components at the (a) C_s and (b) C_{2v} configurations shown in Fig. 1. The total SAPT interaction energy is also shown and compares well with that obtained using CCSD(T)/CBS.

configurations fitted (not shown), generally the errors were small within the region of the potential well and tail. Geometry minimization with the fitted potential (see Table 3) resulted in a global minimum energy structure which was planar (C_{2v}) rather than bent (C_s). In general, it is difficult to reproduce fine features of an intermolecular potential energy surface with simple functional forms like the ones used here. One must compromise between usability of the potential for MD and its complexity. We believe that our fit is accurate for our purpose and comparable to the water potential with which it was matched.

Our potential reproduces the *ab initio* depth of about 2.3 kcal mol^{-1} reasonably well, as shown in Table 3. This is in contrast to ref. 27 and 47 where the authors employed a potential with a depth of only $\sim$1.1 kcal mol^{-1}. However, it must be noted that the NO_2–H_2O portion of that potential was not explicitly fitted for NO_2–H_2O, instead being simply a universal force field extended to NO_2–H_2O.

3.2 Scattering simulations of NO_2 at the air–water interface

In Fig. 4 are shown the 160 trajectories generated in this work while Fig. 5 displays typical trajectories for each of the four possible observed outcomes: direct scattering, adsorption, desorption, and absorption. In this work, an NO_2 molecule is considered to be directly scattered if it leaves the surface after being resident in the vicinity of the surface for only a short duration of less than 2 ps since this is approximately the time needed for dissipation of kinetic energy of a typical thermal impacting molecule into the water surface.[18] An adsorbed molecule is one that remains within the interfacial region for a longer period, for our purposes, about 10 ps. The molecule may later be desorbed from the surface. Such molecules may be considered to be trapped (*i.e.*, not in equilibrium). We consider a molecule to be absorbed if it is in the bulk liquid for 10 ps or more at the end of the 90 ps interval.

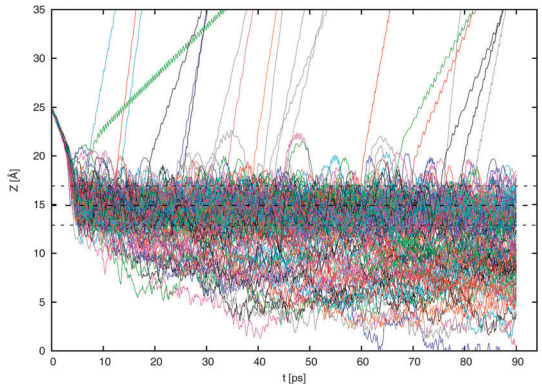

Fig. 4 Results of the 160 scattering simulations. The vertical position of the NO_2 nitrogen atom relative to the center of the water slab is shown as the simulation proceeds. The position of the Gibbs dividing surface Z_{GDS} and its surrounding interfacial width $\pm 2\delta$ are also shown.

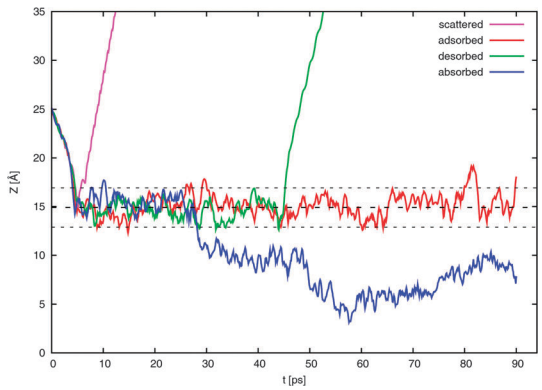

Fig. 5 Like Fig. 4 except here are shown only one typical example of a possible outcome: direct scattering, surface trapping in the form of adsorption and possible later desorption, and absorption.

3.2.1 Direct scattering. In Fig. 5 the directly scattered trajectory shown spends about 4 ps accelerating toward the surface, about 1 ps in the vicinity of the surface, and then is scattered away from the surface at about 5 ps after the start of the simulation.

3.2.2 Trapping at the liquid surface compared to absorption into the bulk. To understand the properties of the trapped state, whether adsorbed or desorbed, and compare them to those of the absorbed state, we conducted longer *NVT* simulations, up to about 0.5 ns, by extending a typical adsorbed trajectory and a typical absorbed trajectory.

Fig. 6 shows a series of (cumulative) snapshots of the nitrogen atom as NO_2 diffuses in the interfacial region (surface and subsurface) of the water slab. It is seen that the whole surface is visited over the course of about 50 ps.

The average orientation of an NO_2 molecule interacting with the surface can be quantified by considering the cosine of the angle between the ONO bisector $\hat{b}$ and the normal to the surface $\hat{Z}$. Note that the dipole moment of NO_2 points in the opposite direction to $\hat{b}$. Fig. 7 shows that an adsorbed NO_2 has a marked orientational preference, with the oxygens pointing into the vacuum, with $\langle\cos(\theta)\rangle$ = 0.40, corresponding to $\hat{b}$ being oriented toward the vacuum at about 66° to the surface normal. As expected, the curve for the absorbed NO_2 shows no orientational preference.

The solvation structure of a solute can be examined quantitatively by considering the radial distribution functions (RDFs) and running coordination numbers (CNs) with respect to the solvent. CN was obtained by integrating the respective RDF curve. The ordinate of the CN curve at the position of the first minimum in the RDF is equal to the number of first-shell solvent molecules surrounding the solute. Fig. 8 compares the RDF $g_{N-O_w}(r)$ and the associated CN of adsorbed and absorbed NO_2. The adsorbed NO_2 has a first solvation shell of waters at a smaller distance than the absorbed NO_2, with the first maximum in $g_{N-O_w}(r)$ being at 3.75 Å and 3.85 Å for the adsorbed and absorbed case, respectively. The corresponding CNs were 6.6 for adsorbed NO_2 and 7.8 for NO_2 in the bulk.

Compared to tetrahedrally coordinated liquid water, the relatively large first shell coordination numbers obtained indicate that NO_2 forms a pocket or cavity on the surface and in the bulk, respectively. Since hydrogen bonds are mostly not present, this volume from which water molecules are excluded is of a relatively large extent. Such behavior is expected given that NO_2 is mildly hydrophobic.

3.2.3 Time evolution of typical outcomes and accommodation coefficients. In Fig. 9 is shown the average time evolution of the four possible outcomes, which are interpreted as evolving

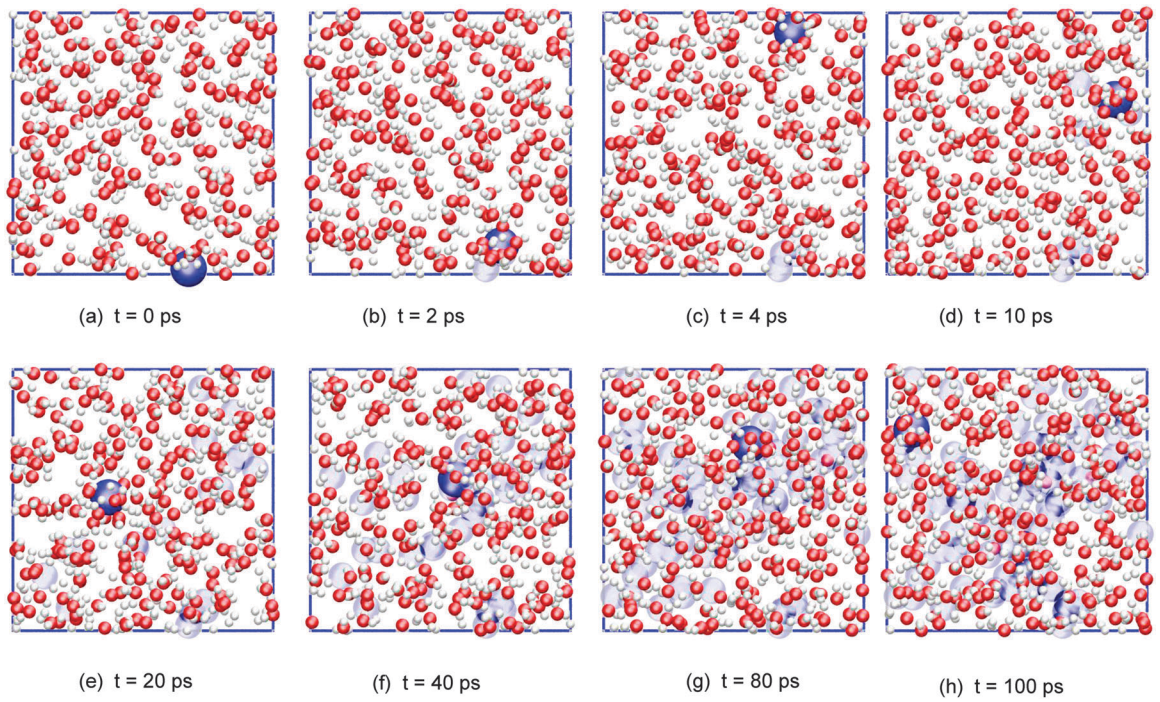

Fig. 6 Cumulative snapshots of a typical adsorbed NO_2 trajectory diffusing along the surface of the water slab (top view; water molecules and, for clarity, only the NO_2 nitrogen atom is shown in dark blue, with its previous positions in light blue).

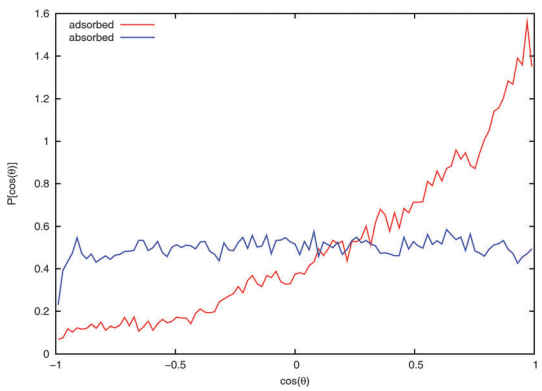

Fig. 7 Probability distribution of NO_2 orientation with respect to the surface normal from extended *NVT* trajectories. If the bisector of NO_2 is aligned with the surface normal then $\cos(\theta) = 1$. Values for NO_2 on the water surface and in the bulk from typical adsorbed and absorbed trajectories, respectively, are shown.

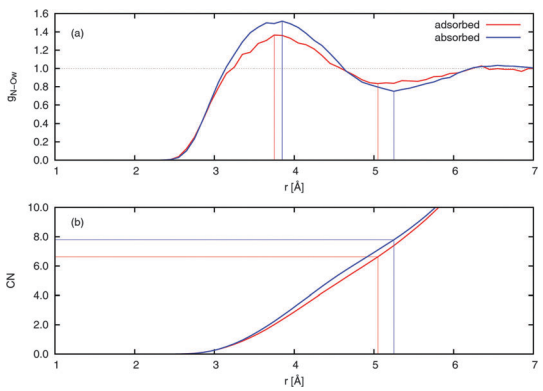

Fig. 8 (a) Radial distribution functions (RDFs) and (b) running coordination numbers (CNs) from extended *NVT* trajectories. Values for NO_2 on the water surface and in the bulk from typical adsorbed and absorbed trajectories, respectively, are shown. A normalization has been imposed so that the RDFs equal unity at large distance, and the CNs have been similarly scaled to match. The lines drawn indicate the position of the first maximum and first minimum in the RDF, the latter enabling determination of the number of nearest-neighbor water molecules surrounding an NO_2 molecule.

time-dependent probabilities. By the end of our simulation period of 90 ps, absorption into the bulk becomes favored over adsorption, and this trend is expected to continue. The probability of desorption slowly increases with time, and in fact will be the determining factor for residence times and the accommodation coefficient, see below.

A calculated accommodation coefficient for NO_2 would be very useful for comparison to the calculated coefficients of other species such as OH obtained in molecular dynamics simulations of similar duration. By counting the fractions of each molecule undergoing these outcomes at the end of the 90 ps period (actually, the average position in the 10 ps interval between 80 and 90 ps), we observed that 2 (or 1% of the 160 trajectories) are directly scattered, 85 (53%) are trapped at the surface [comprised of 66 (41%) adsorbed molecules, with 19 (12%) subsequently desorbed], and 73 (46%) are absorbed. This provides thermal and mass accommodation coefficients of $S_{MD} = 0.99$ and $\alpha_{MD,upper} = 0.87$, respectively. With $p_k = 0.79$, we finally obtain $\alpha_{MD} = 0.78$. With respect to its interaction with water, NO_2 is similar in many respects to OH (which has a calculated mass accommodation coefficient of 0.83; see, *e.g.*, ref. 16–18 and 52). Like OH, NO_2 behaves as a surfactant on water.

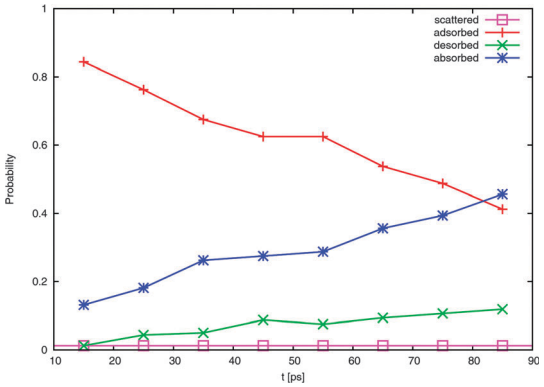

Fig. 9 Evolution of probability with time of the four typical outcomes.

Experimentally measured values of the net uptake coefficient reported previously are summarized in the IUPAC Gas Kinetic Data Evaluation.[53] At 298 K, they range from $<10^{-7}$ to 10^{-3}. This wide range is likely in large part due to varying contributions from reevaporation back into the gas phase on the time scales of the measurements (generally ms or longer). The same issue makes comparison of experimental results to theory problematic, since the time scales in molecular dynamics simulations are typically 100 ps or shorter. Disagreement between calculated and measured uptake of a number of gases at water surfaces is quite common[18,54,55] because of these vastly different time scales.

4 Atmospheric chemistry implications

The importance of reactions of NO_2 at the interface will depend on its surface concentration, which is determined by the rates of uptake and desorption. The results of this study suggest that trapping of NO_2 upon collision with the surface is quite efficient and hence is limited by the gas phase concentration. In addition, our results suggest that the residence time (τ) for NO_2 on the surface is at least of the order of 1 ns, and our estimates suggest that it could be 10 ns or more even on a pure water surface. Under some conditions, concentrations of NO_2 sampled in the plumes from emission sources can be quite high. For example, automobile exhaust collected in Teflon chambers can have concentrations of 30 ppm or more.[56,57] Under these conditions, liquid water is also present either as droplets or adsorbed on the walls of the sampling system and chamber. For 30 ppm NO_2, the collision rate with the surface at 298 K is 6.9×10^{18} s^{-1} cm^{-2}. Taking the rate constant for desorption as 10^8 s^{-1}, corresponding to a residence time on the surface of 10 ns, an NO_2 surface concentration of 6.9×10^{10} cm^{-2} at steady-state is derived.

At an NO_2 surface concentration of 6.9×10^{10} cm^{-2}, there are 1.6×10^{-3} NO_2 in each box, *i.e.*, there would be on average about one NO_2 in 644 of these boxes. As shown in Fig. 6, the mobility of NO_2 on the surface is such that it samples most of the 15 Å × 15 Å box in ~50 ps. Sampling 644 boxes containing on average one NO_2 would take 32 ns, the lower limit for the residence time of NO_2 on the surface. This suggests that the likelihood of two NO_2 molecules colliding and having an opportunity to react to form the dimer, $NO^+NO_3^-$ and subsequently HONO, is high under these conditions. Such a process could be at least in part responsible for the relatively high rates of conversion of NO_2 to HONO observed in such systems. For example, in a Teflon sampling chamber containing auto exhaust from a 1980 pickup truck operated in a standard highway driving cycle, 67 ppm NO_2 and 8.5 ppm HONO were observed, corresponding to a 13% conversion of NO_2 to HONO.[56]

The effective residence time of NO_2 and reactivity may be enhanced beyond that estimated here by several factors. First, although 10 ns is the limit of the present calculations, the true residence time for NO_2 on the surface may be greater than this, giving higher NO_2 surface concentrations and probabilities for reaction with NO_2 or other species. Second, residence times may be increased by interaction with other species in the aqueous phase such as chloride ions, HNO_3 or NO_3^- and some surfactants.[12,13,58–60] We therefore consider the estimates above to be somewhat conservative.

5 Concluding remarks

The minimum energy structure of the NO_2–H_2O complex was characterized by coupled-cluster calculations and found to be of C_s symmetry, with an O_2N–OH_2 bonding pattern. The intermolecular separation and binding energy are typical for a van der Waals complex dominated by the electrostatic interaction. SAPT calculations confirmed that the electrostatics component was dominant. The intermolecular bond can be understood to be driven by a maximization of the dipole–dipole interaction. Nevertheless, the dispersion interaction was significant. Our calculations showed that the complex is twice as strongly bound as calculated by previous researchers.

An intermolecular potential was fitted to SAPT interaction energy points and molecular dynamics simulations of an NO_2 molecule interacting with an air–water interface under ambient conditions were performed. We observed that the bonding pattern of NO_2 to the water molecules was of the aforementioned type; in particular, we did not observe NO_2 forming hydrogen-bonded structures with the water molecules. NO_2 behaved like a small mildly hydrophobic molecule in water, with the oxygens of NO_2 generally not interacting with the water molecules. For NO_2 at the surface of water, this led to a pronounced orientational preference, with the NO_2 oxygens pointing out of the interface. The mildly hydrophobic nature of NO_2 is also suggested by experiments currently underway.

Scattering simulations were performed to determine the typical outcomes of NO_2 encountering the air–water interface. We observed that significant fractions of the trajectories were trapped at the surface or absorbed into the bulk. We suggest that the latter fraction may provide a reservoir of NO_2 molecules for HONO production. Moreover, the observed orientational preference of NO_2 on the surface of the water may imply that the asymmetric dimer, $ONONO_2$, could be directly formed, obviating the need for surmounting of the high barrier[10,61] between symmetric and asymmetric forms.

Due to the limited time scale of our simulations, we cannot make definitive statements on the residence times of NO_2 on the surface or in the bulk. However, there is a marked preference

of NO_2 for becoming trapped in the interface or in the bulk when a time scale of about 100 ps is considered, a time scale which is relevant for chemical interactions to occur.

Acknowledgements

We wish to acknowledge the generous support from the US Department of Energy Office of Science, Grant DE-FG02-09ER64762; and UCI—greenplanet (NSF Grant CHE-0909227) computational facilities and the HUJI—katara computational facilities. The work at the Hebrew University was supported by the Israel Science Foundation, grant number 114/08. GM would like to acknowledge discussions with Madeleine Pincu and Christopher Mundy. We thank James N. Pitts, Jr. for helpful discussions and comments on the manuscript.

References

1 B. J. Finlayson-Pitts and J. N. Pitts, *Chemistry of the Upper and Lower Atmosphere: Theory, Experiments, and Applications*, Academic Press, San Diego, 2000.
2 B. J. Finlayson-Pitts, L. M. Wingen, A. L. Sumner, D. Syomin and K. A. Ramazan, *Phys. Chem. Chem. Phys.*, 2003, **5**, 223–242.
3 J. Stutz, B. Alicke and A. Neftel, *J. Geophys. Res., [Atmos.]*, 2002, **107**, 8192.
4 H. Su, Y. F. Cheng, P. Cheng, Y. H. Zhang, S. Dong, L. M. Zeng, X. Wang, J. Slanina, M. Shao and A. Wiedensohler, *Atmos. Environ.*, 2008, **42**, 6219–6232.
5 Y. Yu, B. Galle, E. Hodson, A. Panday, R. Prinn and S. Wang, *Atmos. Chem. Phys.*, 2009, **9**, 183–223.
6 G. Li, W. Lei, M. Zavala, R. Volkamer, S. Dusanter, P. Stevens and L. T. Molina, *Atmos. Chem. Phys.*, 2010, **10**, 6551–6567.
7 J. Wang and B. E. Koel, *Surf. Sci.*, 1999, **436**, 15–28.
8 J. Wang and B. E. Koel, *J. Phys. Chem. A*, 1998, **102**, 8573–8579.
9 J. Wang, M. R. Voss, H. Busse and B. E. Koel, *J. Phys. Chem. B*, 1998, **102**, 4693–4696.
10 A. S. Pimentel, F. C. A. Lima and A. B. F. da Silva, *J. Phys. Chem. A*, 2007, **111**, 2913–2920.
11 A. S. Pimentel, F. C. Lima and A. B. da Silva, *Chem. Phys. Lett.*, 2007, **436**, 47–50.
12 M. A. Kamboures, J. D. Raff, Y. Miller, L. F. Phillips, B. J. Finlayson-Pitts and R. B. Gerber, *Phys. Chem. Chem. Phys.*, 2008, **10**, 6019–6032.
13 M. A. Kamboures, W. van der Veer, R. B. Gerber and L. F. Phillips, *Phys. Chem. Chem. Phys.*, 2008, **10**, 4748–4753.
14 Y. Miller, B. J. Finlayson-Pitts and R. B. Gerber, *J. Am. Chem. Soc.*, 2009, **131**, 12180–12185.
15 K. A. Ramazan, L. M. Wingen, Y. Miller, G. M. Chaban, R. B. Gerber, S. S. Xantheas and B. J. Finlayson-Pitts, *J. Phys. Chem. A*, 2006, **110**, 6886–6897.
16 M. Roeselova, P. Jungwirth, D. J. Tobias and R. B. Gerber, *J. Phys. Chem. B*, 2003, **107**, 12690–12699.
17 M. Roeselova, J. Vieceli, L. X. Dang, B. C. Garrett and D. J. Tobias, *J. Am. Chem. Soc.*, 2004, **126**, 16308–16309.
18 J. Vieceli, M. Roeselova, N. Potter, L. X. Dang, B. C. Garrett and D. J. Tobias, *J. Phys. Chem. B*, 2005, **109**, 15876–15892.
19 M. Baer, C. J. Mundy, T.-M. Chang, F.-M. Tao and L. X. Dang, *J. Phys. Chem. B*, 2010, **114**, 7245–7249.
20 H. J. C. Berendsen, J. R. Grigera and T. P. Straatsma, *J. Phys. Chem.*, 1987, **91**, 6269–6271.
21 W. S. Benedict, N. Gailar and E. K. Plyler, *J. Chem. Phys.*, 1956, **24**, 1139.
22 S. A. Clough, Y. Beers, G. P. Klein and L. S. Rothman, *J. Chem. Phys.*, 1973, **59**, 2254.
23 Y. Tu and A. Laaksonen, *Chem. Phys. Lett.*, 2000, **329**, 283–288.
24 P. L. Silvestrelli and M. Parrinello, *Phys. Rev. Lett.*, 1999, **82**, 3308–3311.
25 Y. S. Badyal, M.-L. Saboungi, D. L. Price, S. D. Shastri, D. R. Haeffner and A. K. Soper, *J. Chem. Phys.*, 2000, **112**, 9206.
26 *CRC Handbook of Chemistry and Physics, Internet Version*, ed. D. R. Lide, Taylor and Francis, Boca Raton, FL, 87th edn, 2007.
27 A. Galashev and O. Rakhmanova, *Russ. J. Phys. Chem. A*, 2010, **84**, 1364–1368.
28 B. Jeziorski, R. Moszynski and K. Szalewicz, *Chem. Rev.*, 1994, **94**, 1887–1930.
29 A. J. Misquitta, R. Podeszwa, B. Jeziorski and K. Szalewicz, *J. Chem. Phys.*, 2005, **123**, 214103.
30 P. S. Zuchowski, R. Podeszwa, R. Moszynski, B. Jeziorski and K. Szalewicz, *J. Chem. Phys.*, 2008, **129**, 084101.
31 SAPT2008.2, an *ab initio* program for many-body symmetry-adapted perturbation theory calculations of intermolecular interaction energies, written by R. Bukowski, W. Cencek, P. Jankowski, *et al.*, University of Delaware and University of Warsaw, http://www.physics.udel.edu/~szalewic/SAPT/SAPT.html.
32 C. Adamo and V. Barone, *J. Chem. Phys.*, 1999, **110**, 6158.
33 S. G. Lias, *Gas phase ion energetics data*, in *NIST Chemistry WebBook*, ed. W. G. Mallard, NIST Standard Reference Database Number 69, 2011, see http://webbook.nist.gov.
34 H.-J. Werner, P. J. Knowles, G. Knizia, F. R. Manby and M. Schütz, *et al.*, *MOLPRO, version 2010.1, a package of ab initio programs*, 2010, http://www.molpro.net.
35 G. Murdachaew, C. J. Mundy and G. K. Schenter, *J. Chem. Phys.*, 2010, **132**, 164102.
36 T. H. Dunning, *J. Chem. Phys.*, 1989, **90**, 1007–1023.
37 The CP2K developers group, http://cp2k.berlios.de/, 2000–2012.
38 I.-F. W. Kuo and C. J. Mundy, *Science*, 2004, **303**, 658–660.
39 I.-F. W. Kuo, C. J. Mundy, B. L. Eggimann, M. J. McGrath, J. I. Siepmann, B. Chen, J. Vieceli and D. J. Tobias, *J. Phys. Chem. B*, 2006, **110**, 3738–3746.
40 G. Murdachaew, C. J. Mundy, G. K. Schenter, T. Laino and J. Hutter, *J. Phys. Chem. A*, 2011, **115**, 6046–6053.
41 J.-P. Ryckaert, G. Ciccotti and H. J. Berendsen, *J. Comput. Phys.*, 1977, **23**, 327–341.
42 G. J. Martyna, M. L. Klein and M. Tuckerman, *J. Chem. Phys.*, 1992, **97**, 2635–2643.
43 D. J. Tobias, G. J. Martyna and M. L. Klein, *J. Phys. Chem.*, 1993, **97**, 12959–12966.
44 D. W. Ball, *Chem. Phys. Lett.*, 1999, **312**, 306–310.
45 A. Chou, Z. Li and F.-M. Tao, *J. Phys. Chem. A*, 1999, **103**, 7848–7855.
46 Y. V. Novakovskaya, D. S. Bezrukov and N. F. Stepanov, *Int. J. Quantum Chem.*, 2004, **100**, 460–468.
47 A. Galashev and O. Rakhmanova, *Colloid J.*, 2010, **72**, 478–485.
48 S. Grimme, *J. Comput. Chem.*, 2006, **27**, 1787–1799.
49 CFOUR, a quantum chemical program package written by J. F. Stanton, J. Gauss, M. E. Harding and P. G. Szalay, *et al.* For the current version, see http://www.cfour.de.
50 M. Valiev, E. Bylaska, N. Govind, K. Kowalski, T. Straatsma, H. Van Dam, D. Wang, J. Nieplocha, E. Apra, T. Windus and W. de Jong, *Comput. Phys. Commun.*, 2010, **181**, 1477–1489.
51 A. Halkier, T. Helgaker, P. Jørgensen, W. Klopper, H. Koch, J. Olsen and A. K. Wilson, *Chem. Phys. Lett.*, 1998, **286**, 243–252.
52 R. Vacha, P. Slavicek, M. Mucha, B. J. Finlayson-Pitts and P. Jungwirth, *J. Phys. Chem. A*, 2004, **108**, 11573–11579.
53 IUPAC Subcommittee for Gas Kinetic Data Evaluation, Data Sheet VI.A1.3, last evaluated April, 2011, http://www.iupac-kinetic.ch.cam.ac.uk/.
54 P. Davidovits, C. E. Kolb, L. R. Williams, J. T. Jayne and D. R. Worsnop, *Chem. Rev.*, 2006, **106**, 1323–1354.
55 B. C. Garrett, G. K. Schenter and A. Morita, *Chem. Rev.*, 2006, **106**, 1355–1374.
56 J. N. Pitts, *Environ. Health Perspect.*, 1983, **47**, 115–140.
57 J. N. Pitts, H. W. Biermann, A. M. Winer and E. C. Tuazon, *Atmos. Environ.*, 1984, **18**, 847–854.
58 S. Enami, M. R. Hoffmann and A. J. Colussi, *J. Phys. Chem. B*, 2009, **113**, 7977–7981.
59 T. Kinugawa, S. Enami, A. Yabushita, M. Kawasaki, M. R. Hoffmann and A. J. Colussi, *Phys. Chem. Chem. Phys.*, 2011, **13**, 5144–5149.
60 A. Yabushita, S. Enami, Y. Sakamoto, M. Kawasaki, M. R. Hoffmann and A. J. Colussi, *J. Phys. Chem. A*, 2009, **113**, 4844–4848.
61 D. de Jesus Medeiros and A. S. Pimentel, *J. Phys. Chem. A*, 2011, **115**, 6357–6365.

